Full-Brillouin-zone calculation of high-order harmonic generation from solid-state media

J. Gu and M. Kolesik

James Wyant College of Optical Sciences, The University of Arizona, Tucson, Arizona 85721, USA

Solid-state high-order harmonic generation (HHG) continues to attract a lot of interest. From the theory and simulation standpoint, two issues are still open; The first is the so-called transition-dipole phase problem. It has been recognized that the dipoles must be treated as complex-valued quantities and that their corresponding Berry connections must be included to ensure phase-gauge invariance. However, while this has been successfully implemented for lower-dimensional systems, fully vectorial and three-dimensional simulations remain challenging. The second issue concerns the symmetry of the high-order harmonic response, when simulations sometimes fail to honor the symmetry of the crystalline material. This work addresses both of these problems with the help of a HHG-simulation approach which (a) is manifestly free of the transition-dipole phase problem, (b) does not require calculation of dipole moments, (c) can account for the contributions from the entire Brillouin zone, and (d) faithfully preserves the symmetry of the simulated crystalline material. We use the method to show that high-order harmonic sources are distributed throughout the Brillouin zone with various phase shifts giving rise to significant cancellations. As a consequence, for the simulated response to correctly capture the material symmetry, contributions from the entire Brillouin zone must be included. Our results have important implications for a number of HHG applications, including all-optical band and dipole reconstruction.

I. INTRODUCTION

High-order harmonic generation (HHG) in solid-state media has been studied with keen interest ever since the first observations a decade ago [1] followed by experiments with many different materials and structures [2,3]. Mediated by the light-matter interactions at high density, the phenomenon opens a new window into the dynamics of the solid-state medium at attosecond timescales, including all-optical reconstruction of the band structure [4–6], mapping of the transition-dipole moments [7], characterization of higher-order nonlinearity [8], and measurements of Berry curvatures [9].

Numerical simulations have played an important role in this field [2,10,11]. The broad spectrum of applied approaches ranges from the *ab initio* time-domain Schrödinger equations [12], multiscale time-domain density-functional theory [13], through many variants of the semiconductor Bloch equations (SBEs) and density-matrix methods [11,14–16], to the studies including propagation effects [17] and coupling with Maxwell equations [13,18–20].

One of the issues that attracted attention over the last few years is that of the transition-dipoles. It concerns the phase-gauge degree of freedom in the description of the electronic Bloch states; they can be modified by arbitrary phase factors [2,11,21] which in turn change the complex phase of the off-diagonal dipole-matrix elements. Closely related to this is the Berry connection which, assuming that Bloch-states are differentiable, gives a gauge-dependent measure of how the Bloch basis changes from one point to the next over the Brillouin zone.

While semiconductor Bloch equations are phase-gauge invariant [22], some early simulations broke this symmetry with the dipole moments treated as real-valued quantities (see discussions in Refs. [23–25]). Moreover, Berry connections [2,11] are still often neglected, which also breaks the gauge-invariance of SBEs. The proper treatment requires the construction of a differentiable [21] and Brillouin-zone periodic phase-gauge [26]. Imposing such a phase-gauge have been demonstrated in one-dimensional models, but doing the same in three-dimensional reciprocal space have not been shown explicitly yet. At any rate, the fact that the Berry connections and dipole-moment phases need careful attention makes the simulation of the HHG from crystals even more difficult—this is what we refer to as the transition-dipole phase (TDP) problem.

Another issue complicating the modeling is that in principle all states from the Brillouin zone contribute to HHG. Currently only a few approaches account for the full three-dimensional Brillouin zone (see, e.g., Refs. [12,13,19,27–29]), and this requires extreme computational efforts. In contrast, most of the modeling to date has been done with lower-dimensional spaces such as straight paths across the center of the Brillouin zone, raising the question of whether the chosen subset really dominates the HHG process [30]. Efficient methods which include all Bloch states are therefore needed.

Intimately related to these two problems is the issue of the symmetry. Clearly, at least for the low excitation intensity the simulated medium response must have the symmetry dictated by the space group of the crystal. For example, the simulated second-order nonlinear tensor must exhibit "hard

zeros" where the symmetry implies vanishing components. This sometimes proved problematic (see, e.g., Refs. [24,25] for a discussion and references therein), when earlier simulations failed to produce and/or to suppress even harmonics as required by the symmetry of the problem.

One of the goals of this work is to put forward a HHG-simulation approach which addresses these issues. It is designed with the recognition that the phase problem is very much self-imposed, it is in fact not required by physics and can be bypassed [31]. By eliminating any and all phase-gauge dependencies, the resulting method (i) is manifestly free of the TDP-problem because it does not require dipole moments or the Berry connection in the first place, (ii) it can efficiently add up the HHG contributions from the full Brillouin zone, and (iii) it automatically produces the response with the correct symmetry. It should be emphasized that the algorithm, while oblivious to Berry connections and to transition dipoles, does not neglect them. Instead, it can work with arbitrary phases implicitly assigned to the band-structure states. In this respect, the approach is distinctly different from other treatments of the TDP issue, including the Wannier representation [31].

It is important that the algorithm we put forward does not depend on the nature of the model to calculate the band structure. All that is required is the ability to obtain the energy eigenvalues and the corresponding eigenvectors for a vector from the Brillouin zone, together with an assumption of the minimal coupling to the electromagnetic field.

We utilize the SBE simulation tool to gain insight into how the HHG is sourced across the Brillouin zone. We show that significant destructive interferences can occur between the HHG contributions originating from distant parts of the Brillouin zone. Moreover, it is not always the case that the regions with the strongest dipoles dominate the generated radiation. These observations imply that simplified models based on one-dimensional subsets of the reciprocal space must be treated with extreme caution, while the full three-dimensional (3D) approach should be preferred whenever computationally feasible.

While ours is not the first simulation which can account for the whole Brillouin zone, the speed and accuracy of the method makes it much more practical to study a number of open problems in the solid-state HHG field (e.g., see review [32]), such as the carrier-envelope phase and propagation effects, perturbative-nonperturbative transitions [33], the role of distinct features in the band-structure [29], higher-energy band gaps [28], and sample-orientation [34] and polarization dependencies [35] in the HHG.

II. SEMICONDUCTOR BLOCH EQUATIONS

Semiconductor Bloch equations [14–16] represent one of the most frequently utilized approaches to the high-order harmonic generation in solid-state media [11]. For the sake of completeness, we review the most important components of the method in this section. We choose to follow Ref. [36] by Wilhelm *et al.* and refer the reader to this well-rounded exposition for details.

It is assumed for this work that the excitation by an optical pulse is at mid-infrared or longer wavelength for which the interaction with the material can be considered off-resonance.

Consequently, the Coulomb interactions play a lesser role [37] and are neglected in what follows. Note that this may not be justified for effectively two-dimensional materials [38], but HHG from bulk crystals is often treated this way.

Assuming that the band-structure of the material is known throughout the Brillouin zone, let $\epsilon_n(\mathbf{k})$ with $n = 1, \ldots, N_b$ describe the N_b energy bands with corresponding eigenvectors $\{|n\mathbf{k}\rangle\}$. The quantum state of the system is given by the density matrix $\rho_{mn}(\mathbf{k}; t)$ with $\mathbf{k}$ running over the Brillouin zone. The initial condition before the excitation pulse arrives is approximated by the zero-temperature density matrix with all conduction bands completely empty and valence bands full.

A. Evolution equations for the density matrix

The SBE system constitutes a set of coupled differential equations, which can be represented in a number of equivalent ways and gauges (described in a recent tutorial by Yue and Gaarde [11]). Here it is written in the time-dependent basis $\{|n\mathbf{k}_t\rangle\}_n$ as an evolution equation for the density matrix $\rho_{nm}(\mathbf{k}; t)$,

$$
[i\partial_t - \epsilon_{nm}(\mathbf{k}_t)]\rho_{nm}(\mathbf{k}; t)
$$
$$
= \mathbf{E}(t) \sum_a [\rho_{na}(\mathbf{k}; t)\mathbf{d}_{am}(\mathbf{k}_t) - \mathbf{d}_{na}(\mathbf{k}_t)\rho_{am}(\mathbf{k}; t)], \quad (1)
$$

where the dipole-moment matrix

$$
\mathbf{d}_{am}(\mathbf{k}_t) = \langle a\mathbf{k}_t | i\partial_{\mathbf{k}_t} | m\mathbf{k}_t \rangle \quad (2)
$$

and the band-energy differences

$$
\epsilon_{nm}(\mathbf{k}_t) = \epsilon_n(\mathbf{k}_t) - \epsilon_m(\mathbf{k}_t) \quad (3)
$$

are calculated for the time-dependent $\mathbf{k}$ vector

$$
\mathbf{k}_t = \mathbf{k} - \mathbf{A}(t), \quad (4)
$$

reflecting the effect of the electromagnetic vector potential $\mathbf{A}(t)$ of the excitation pulse. For the moment, dephasing terms are omitted for the sake of simplicity—they will be included later.

Equations (1) to (4) are in the velocity gauge. One advantage over their counterpart in the length gauge is that the latter contains gradients which result in a coupling between equations for different $\mathbf{k}$. This version is therefore easier to parallelize with a near-perfect load balance. Because we integrate the evolution for all relevant Bloch states, the parallel efficiency is an important aspect to consider.

B. Observables

Once the evolution system is integrated for all $\mathbf{k}$, the induced current density is calculated by integrating the Brillouin zone and adding contributions from all bands [formula (62) in Ref. [36]] like so:

$$
\mathbf{j}(t) = \sum_{mn} \int \frac{d\mathbf{k}}{(2\pi)^3} \langle n\mathbf{k}_t | \partial_{\mathbf{k}_t} h(\mathbf{k}_t) | m\mathbf{k}_t \rangle \rho_{mn}(\mathbf{k}; t). \quad (5)
$$

Here, $h(\mathbf{k})$ is the instantaneous Hamiltonian with eigenstates $\{|n\mathbf{k}\rangle\}$ corresponding to the given $\mathbf{k}$ vector, and $\partial_{\mathbf{k}} h(\mathbf{k})$ is the Hamiltonian-matrix gradient in the reciprocal space. Note that the current density can be separated into various components

[36], including inter- and intraband contributions [39] for more physical insight, but this is not pursued here.

With the current density coupled to Maxwell equations, "all one needs to do" to simulate high-order harmonic generation in a medium exposed to an electromagnetic pulse is to integrate the Maxwell-SBE system. However, the above equations were derived with certain assumptions which bring complications. One has to evaluate the dipole moment operator (2) which obviously requires $|m\mathbf{k}\rangle$ to be differentiable with respect to $\mathbf{k}$. This is where the transition-dipole phase issue comes in.

III. TRANSITION-DIPOLE PHASE

There is an extensive literature dealing with the so-called transition-dipole phase (TDP) problem (see, e.g., Ref. [26]). Not long ago, in the early simulations of HHG from solids, the fact that the dipole moment as a function of the $\mathbf{k}$ vector is a complex-valued quantity was ignored and only the absolute values were utilized in the calculations. The state of the art improved in recent years, and the community has a good understanding of these issues [11]. Nowadays there is a consensus that the "transition-dipole phase plays a role" in HHG (see, e.g., Refs. [23–25]), but we feel it is useful to emphasize that the *absolute phase* of any dipole matrix element is not a measurable quantity. This is why we want to include a very brief review here.

A. Gauge invariance

Let us start with the origin of the TDP problem. In quantum theory, the state of a system is represented not by a vector, as it is often inaccurately described in the physics literature, but by a ray which is a one-dimensional subspace of the Hilbert space (see, e.g., Refs. [40,41]). In other words, after multiplication by an arbitrary nonzero complex number, the vector still stands for the exactly same physical state. This means that, as $\mathbf{k}$ runs over the Brillouin zone, bases $\{|n\mathbf{k}\rangle\}$ can be replaced by ones which differ by arbitrary phase factors on each of their elements, $\{e^{i\phi_n(\mathbf{k})}|n\mathbf{k}\rangle\}$, where the phase $\phi_n(\mathbf{k})$ can be anything, including nondifferentiable, noncontinuous, or even completely random.

Any change in the chosen phase of the basis vectors by $\phi_n(\mathbf{k})$ modifies the transition dipole (2)

$$\mathbf{d}_{am}(\mathbf{k}) \rightarrow e^{-i\phi_a(\mathbf{k})}\langle a\mathbf{k}|i\partial_{\mathbf{k}}|m\mathbf{k}\rangle e^{+i\phi_m(\mathbf{k})}, \qquad (6)$$

which makes it evident that the SBE system in fact *assumes* that the phases of the basis vectors throughout the Brillouin zone were *chosen* such that the resulting dipole moments are differentiable. This has been called differentiable gauge, and one usually adds a requirement that the dipoles are also made Brillouin-zone periodic.

Of course, changing the gauge also modifies the off-diagonal elements of the density matrix. However, once the physical observables are calculated as, e.g., in (5) the choice of the phases gets completely "erased." This is a manifestation of the phase-invariance of the SBE system which has been shown via explicit calculations for various SBE-representations [22]. The same conclusion can be obtained already from the basic principles of the quantum mechanics. Indeed, since the phase-modified basis vectors represent the same physical states, observable quantities are always completely independent of how $\phi_n(\mathbf{k})$ may be set. Thus, there is no measurement which could reveal the absolute phase of a vector or of a matrix element, including that of the dipole moment (2). This does not mean that the dipole moment phase can be set arbitrarily because one only has $N_b - 1$ free parameters to adjust phases of $N_b(N_b - 1)/2$ off-diagonal elements of $\mathbf{d}_{am}(\mathbf{k})$.

B. Numerical issues

Before running a HHG simulation based on the SBE, one must obtain the dipole moments. Density-functional theory (DFT) software are most often used to calculate the band structure of a material and they can also provide the dipole matrices. No matter what kind of a solver is used to diagonalize the model Hamiltonian, the resulting eigenstates calculated for two nearby $\mathbf{k}$ vectors may or may not end up close to each other. In particular, the phases of the bases obtained at different location inside Brillouin zone may appear "random" (although in practice they are not truly random). For this reason, algorithms to generate a "smooth periodic phase" have been developed [26]. It is relatively straightforward to obtain a smooth phase along a one-dimensional subspace of the Brillouin zone, and it can also be arranged to have a desired periodicity. However, to the best of our knowledge the methods were not yet explicitly demonstrated for the three-dimensional reciprocal space.

Another consideration relevant for the numerical treatment is the calculation of the off-diagonal dipole moments and of the Berry connection which is the diagonal part of $\mathbf{d}_{am}(\mathbf{k})$. The off-diagonal part can be obtained without numerical differentiation [36], but this depends on expressions which become numerically inaccurate when close to degeneracy. Nevertheless, since it is possible to avoid numerical differentiation for the off-diagonal dipoles, one may wonder if the SBE representation (1), which does not feature any gradients, needs to care about the dipole phase at all; is it perhaps possible to execute the simulation with whatever phases were given to the dipoles by the eigensolver? The answer would be affirmative if not for two serious issues: (i) Extremely poor accuracy around sharp "phase jumps" (which are guaranteed to occur) and, more importantly, (ii) the diagonal part, i.e., the Berry connection, which is a gauge-dependent quantity.

The inclusion of the Berry connection is crucial for maintaining the phase invariance of the system [22]. One reason it was possible to ignore it in many simulations is that leaving out Berry connection may still produce a reasonably looking high harmonic spectrum. Nevertheless, such results are incorrect because they depend on the nonphysical (as in unobservable) phase choice for the Hamiltonian bases. Numerical evaluation of Berry connections involves "comparison" of Hamiltonian bases at nearby $\mathbf{k}$ vectors. This calculation is essentially similar to numerical differentiation and it may require an extremely fine grid in the $\mathbf{k}$ vector space.

To summarize this section, once we have committed to simulate the SBE-system (1) or its gauge-related counterparts (see Ref. [36]) in the precise form as written, we must address the problem of the smooth, Brillouin-zone periodic phases assigned to the states of the material band structure. Moreover,

we need to evaluate the transition dipole matrix elements and the Berry connection which brings a set of further numerical challenges. This begs the question if all of this is really necessary, because the requirement of the differentiable TDP is "self-inflicted" by the choice of assumptions underlying (1). Quantum theory says that, for any observable quantity, *all phase choices are equivalent*, so one could design the SBE solver to be "phase-choice oblivious." This is demonstrated next.

IV. SEMICONDUCTOR BLOCH EQUATION SOLVER ALGORITHM

To lay out the idea of the algorithm, it would be useful to appreciate the roles played by the different terms in the SBE system (1). Detailed derivations, as shown, e.g., in Refs. [11,36], make it evident that the part proportional to the electric field originates from the time-dependent basis. Even a constant solution appears to depend on time when a time-dependent basis is used, and it is this that the term accomplishes upon integration. Namely, it smoothly transforms the density matrix from the Hamiltonian basis at time t_1 to a different basis at time t_2. So if it is sufficient to know the solution only at these discrete points in time, we can transform the density matrix with a unitary matrix in a single step, and thus skip all the work needed to solve the system of ordinary differential equations and avoid accumulation of numerical errors at the same time.

To demonstrate that we get the correct solution, consider the right-hand side of (1) between times t_i and t_{i+1} and construct the following unitary matrix:

$$U_{ab}(t) = \langle a\mathbf{k}_t | b\mathbf{k}_i \rangle, \tag{7}$$

with

$$\mathbf{k}_t = \mathbf{k} - \mathbf{A}(t) \text{ and } \mathbf{k}_i = \mathbf{k} - \mathbf{A}(t_i). \tag{8}$$

Next, calculate

$$\rho(t) = U(t)\rho(t_i)[U(t)]^\dagger \tag{9}$$

for $t_i < t < t_{i+1}$, and differentiate it with respect to t to obtain,

$$i\dot{\rho}(t) = i\dot{U}(t)\rho(t_i)[U(t)]^\dagger + iU(t)\rho(t_i)[\dot{U}(t)]^\dagger. \tag{10}$$

Inserting $I = UU^\dagger = U^\dagger U$ between the constant $\rho(t_i)$ and the dotted (time-differentiated) operators and subsequently using (9) we get

$$i\dot{\rho}(t) = i\dot{U}(t)[U(t)]^\dagger \rho(t) + i\rho(t)U(t)[\dot{U}(t)]^\dagger. \tag{11}$$

Using $\dot{U}U^\dagger = -U\dot{U}^\dagger$ one obtains the right-hand side in the form of a commutator,

$$i\dot{\rho}(t) = i\dot{U}(t)[U(t)]^\dagger \rho(t) - i\rho(t)\dot{U}(t)[U(t)]^\dagger, \tag{12}$$

which is to be compared with that in (1), so we want to expand $\dot{U}U^\dagger$. The time derivative of the transformation matrix is

$$\dot{U}_{ab}(t) = \partial_t \langle a\mathbf{k}_t | b\mathbf{k}_i \rangle = \mathbf{E}(t) \cdot \langle \partial_{\mathbf{k}_t} a\mathbf{k}_t | b\mathbf{k}_i \rangle, \tag{13}$$

and $\dot{U}U^\dagger$ reveals the dipole moment and the electric field,

$$i\dot{U}_{ab}(U^\dagger)_{bc} = i\mathbf{E}(t) \cdot \langle \partial_{\mathbf{k}_t} a\mathbf{k}_t | b\mathbf{k}_i \rangle \langle b\mathbf{k}_i | c\mathbf{k}_t \rangle$$
$$= -\mathbf{E}(t) \cdot \langle a\mathbf{k}_t | i\partial_{\mathbf{k}_t} c\mathbf{k}_t \rangle = -\mathbf{E}(t) \cdot \mathbf{d}_{ac}(\mathbf{k}_t). \tag{14}$$

Using this in (12) gives

$$i\dot{\rho}_{nm} = \mathbf{E}(t) \sum_a [\rho_{na}\mathbf{d}_{am}(\mathbf{k}_t) - \mathbf{d}_{na}(\mathbf{k}_t)\rho_{am}], \tag{15}$$

which is precisely the **E**-field term in (1). Thus, the basis transformation (7) would give an exact solution if not for the diagonal part of the SBE system. Because the exact solution can be also obtained for the diagonal part, Eq. (1) is a natural candidate for the operator-splitting approach.

Let us assume that the evolution of the system is sampled on a discrete grid of times, t_i, and let $\mathbf{k}_i$ stand for $\mathbf{k}_t$ calculated for $t = t_i$. Furthermore, let $\{|m\mathbf{k}_i\rangle\}_{m=1}^{N_b}$ be the Hamiltonian eigenbasis at time t_i and use it with whatever phases an eigensystem solver assigned to the eigenvectors. The basis transformation between $t_i \rightarrow t_{i+1}$ is given by the unitary matrix

$$U_{ab}^{(i)} = \langle a\mathbf{k}_{i+1} | b\mathbf{k}_i \rangle, \tag{16}$$

and this is used as in (9) to evolve the density matrix from t_i to t_{i+1}.

The other split operator is diagonal; it represents the adiabatic evolution in the time-dependent basis. Joining the two split-operator actions together, the density-matrix evolution over the time-step interval $\Delta t = t_{i+1} - t_i$ can be approximated by

$$\rho(t_{i+1}) = P^{(i)}\rho(t_i)(P^{(i)})^\dagger, \tag{17}$$

where the evolution operator is

$$P_{ab}^{(i)} = e^{-i\epsilon_a(\mathbf{k}_i)\Delta t/2} U_{ab}^{(i)} e^{-i\epsilon_a(\mathbf{k}_i)\Delta t/2}. \tag{18}$$

This operator-splitting formula is locally second-order accurate [42], but that alone tells us little about how long Δt can be. At any rate, the permissible integration step depends on the electric-field intensity and it must be established in a case-by-case convergence study. For the simulation results presented in this work the time step was $\Delta t = 0.07$ fs.

To complete one integration step, the phenomenological damping can be included between the split steps by appropriate modification of the off-diagonal parts of the density matrix [11]. We used a dephasing time of five femtoseconds for our examples in Sec. VI.

Since we have not assumed anything about the phase relations between the bases at t_i and t_{i+1}, the Hamiltonian eigenstates can be used as calculated by the eigensystem solver, and this algorithm is manifestly free of the transition-dipole phase problem. As a sanity check, we have inserted in the numerical evolution scheme a procedure which generates and assigns truly random phases to all Hamiltonian eigenvectors after each and every call to the eigensystem solver—with no significant change in observables.

The fact that we can work with *any* eigenvector phases including random ones is a crucial advantage over the approaches which rely on the numerical integration of SBE using ODE-solvers. An additional important benefit is that this algorithm does not require calculation of the dipole-moment matrix elements. Given that accurate dipole calculations are challenging, this feature alone eliminates the most significant source of numerical noise and makes it possible to calculate HHG spectra with the dynamic range well beyond what is typical for the traditional approach.

V. HIGH-ORDER HARMONIC GENERATION IN ZINC-BLENDE MATERIALS

To illustrate the capabilities of the SBE-solver algorithm described in the previous sections, we present simulations of high-order harmonic generation in zinc-blende structures, choosing GaAs and ZnSe for our examples.

A. Material model

As for the choice of the material model, most of the HHG simulations utilize DFT calculations to obtain the material band-structure and related quantities such as dipole moments. While the method described above is in principle applicable with any material description capable of producing Hamiltonian eigenstates for any **k** throughout the Brillouin zone, for this work we prefer to use tight-binding models. One could argue that such a description is less accurate in terms of the band structure, and it is a valid point. On the other hand, SBE-based simulations using DFT-based material model over a three-dimensional Brillouin zone has yet to be demonstrated. Moreover, the results from DFT calculations suffer from numerical issues, for example, it may be difficult to tell apart Bloch states which are energetically close from truly degenerate states. Because we concentrate on qualitative properties of the HHG, for this work we choose the tight-binding description which is free of such numerical issues. Given that the theory-experiment comparisons are still qualitative rather than quantitative in the field of solid-state high-order harmonic generation, we believe that these models will be useful in their own right for a number of computer-aided studies.

We have used the empirical tight-binding models to obtain the quantities required by the solver, i.e., the **k**-dependent Hamiltonian $h(\mathbf{k})$ built on the frequently used sp^3s^* model [43,44]. For simplicity, we neglect the spin-orbit coupling and include ten bands. The explicit form of the Hamiltonian matrix and its parametrization can be found in Ref. [45]. Exact diagonalization procedure is executed "on the fly" as needed for any given **k**, producing the set of eigenvectors $|m\mathbf{k}\rangle$ and band energies $\epsilon(\mathbf{k})$. For the calculation of the current density (5), the vector matrix $\partial_\mathbf{k}h(\mathbf{k})$ is also calculated exactly from the model. Thus, there is no interpolation or any finite-difference approximations needed.

Needless to say, repeated diagonalization on the fly would be impractical should one want to use first-principle calculations, such as DFT, to obtain the material properties. However, localized Wannier functions [46] can be used to transform *ab initio* calculation into an effective tight-binding Hamiltonian [31,47], and this then can be used in our algorithm in the same way as we do in our illustrations.

It should also be emphasized that the on-demand diagonalization is not a requirement in our method. For the readers who may want to use the algorithm with other than tight-binding material descriptions, and especially with methods relying on *ab initio* calculations, we outline in the Appendix an implementation using precalculated material data.

B. Pulsed excitation

The examples given next assume excitation by a linearly polarized pulse with the central wavelength of $\lambda = 3.6$ μm,
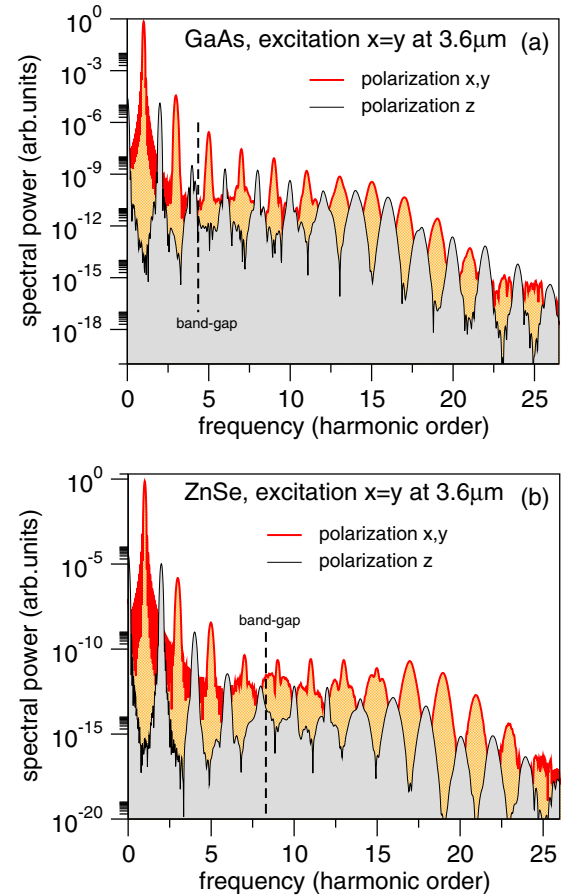

FIG. 1. High-order harmonic generation in crystals excited by a linearly polarized pulse oscillating along the $x = y$ (crystal) direction.

envelope duration of 100 fs ($\cos^2$ shape), and a field intensity of 8.7×10^8 V/m. We explore different crystal orientations to demonstrate that the nonlinear response exhibits the expected orientation and polarization properties. As propagation effects [17] are not studied in this work, the observable of interest is the vector of the current density calculated for the given excitation pulse.

C. High-order harmonic generation spectra from the whole Brillouin zone

For the first example we consider a crystal sample oriented such that the linearly polarized pulse oscillates along direction (1,1,0), i.e., perpendicular to the crystal z axis. In this geometry, the material symmetry dictates that the second-harmonic response only appears in the z direction. This is because the second-order tensor $\chi^{(2)}_{abc}$ of the zinc-blende structure vanishes unless all a, b, c are different. In contrast, the third harmonic excited by the Kerr effect is expected to show up along the $x = y$ direction.

Figure 1 depicts the simulated HHG spectra for GaAs and ZnSe samples and shows that the polarization properties are indeed as one expects, with even and odd harmonics separated between the parallel and perpendicular polarizations.

We have intentionally used a relatively long duration pulse so that the well-separated harmonics showcase that the
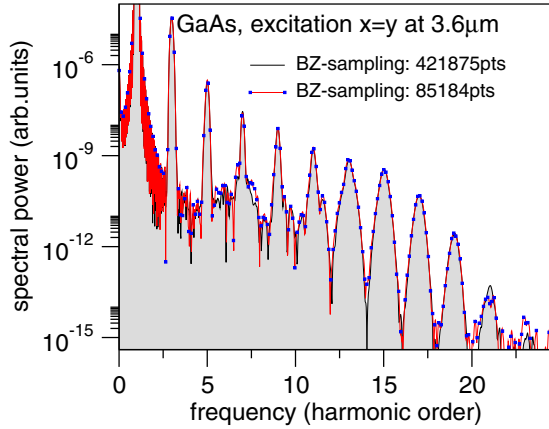
FIG. 2. Convergence of the numerical HHG spectra for two different numbers of sampling points in the 3D Brillouin zone.

FIG. 4. Orientation-dependent high-order harmonic generation in a 110-oriented GaAs crystal. (left) Simulated second harmonic filtered from the current density in the parallel (p) and perpendicular (s) polarizations shown as functions of the sample rotation angle. (right) The second-harmonic radiation pattern for the zinc-blende nonlinear tensor.

calculated spectra are free of the noise floor so typical of many HHG simulations—here the noisy background occurs about ten orders of magnitude below the lower edge of these plots. This indicates the excellent numerical fidelity of the algorithm.

The question of convergence is obviously important. Making sure that the time step is short enough and does not affect the convergence, we compare the spectra simulated with different number of sampling points in the Brillouin zone. Figure 2 shows an example where convergence is achieved over a dynamic range of fifteen orders of magnitude.

To show a case when both even and odd harmonics appear simultaneously in the parallel and perpendicular polarizations, we include Fig. 3. Although we do not actually propagate the excitation pulse, we assume that the sample orientation is 110 and then rotate the sample about the beam axis as it is often done in experiments. In this figure the sample is rotated by 45 degrees, and we look at the current density polarized parallel (p) and perpendicular (s) to the polarization direction of the excitation pulse. In this particular case, the even harmonics, while clean and well defined, are weaker

than the odd harmonics and this is especially the case for the p-polarized component.

The relative strength between the odd and even harmonics depends on the angle of the sample rotation. This is illustrated in Fig. 4 for the second-harmonic frequency band. The radiation pattern (left) is essentially the same as expected from the classical $\chi^{(2)}$ tensor of the zinc-blende structure (right), and this corroborates that the simulated response has the correct symmetry. It should be interesting to study the deviations from the classical (equilibrium) predictions based on a fixed $\chi^{(2)}$ as a function of the excitation pulse intensity, but we will not pursue this here.

For a more difficult-to-pass test of the symmetry properties of the simulated high-order harmonics, Fig. 5 shows the results for the excitation with a pulse polarized along one of the crystal axes (x). In this case the response components z and y are supposed to vanish and indeed they do. The z component shows up in these plots as a noisy background (gray area below the black curve) about fifteen orders of magnitude below the level of the x-polarized signal. One could say that this is nothing but a simple sanity check because our SBE-based simulation automatically inherits the correct symmetry properties from the material model. Nevertheless, it is important to note that the "numerical zero" demonstrated for the current components which are forbidden by symmetry does not occur point by point (in the reciprocal space). Instead, all regions throughout the Brillouin zone contribute nonzero signals, and the symmetry appears only after significant (or complete in the case here) cancellations. Because of their important implications, we discuss these issues next.

D. Mapping the Brillouin zone for the high-order harmonic generation source

One often-utilized simplification in the solid-state HHG simulations is that, instead of the entire Brillouin zone only a one-dimensional line is used to represent the reciprocal space. We now present a few examples which demonstrate that a great deal of caution is in order when trying to interpret HHG-simulation results based on a low-dimensional subset of the reciprocal space because

(a) the source of the high-order harmonics is distributed throughout the entirety of the Brillouin zone, and
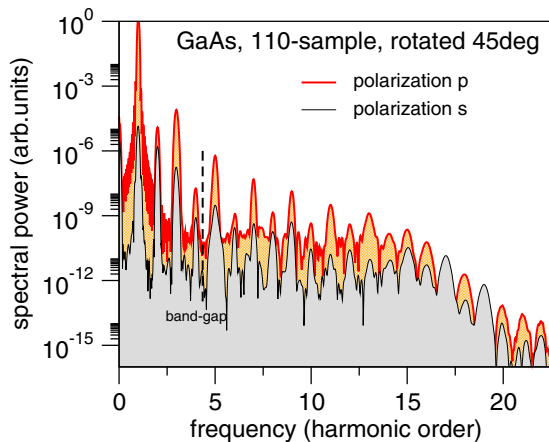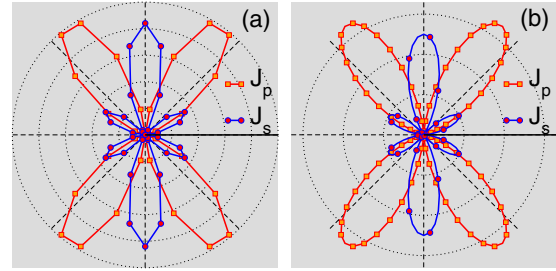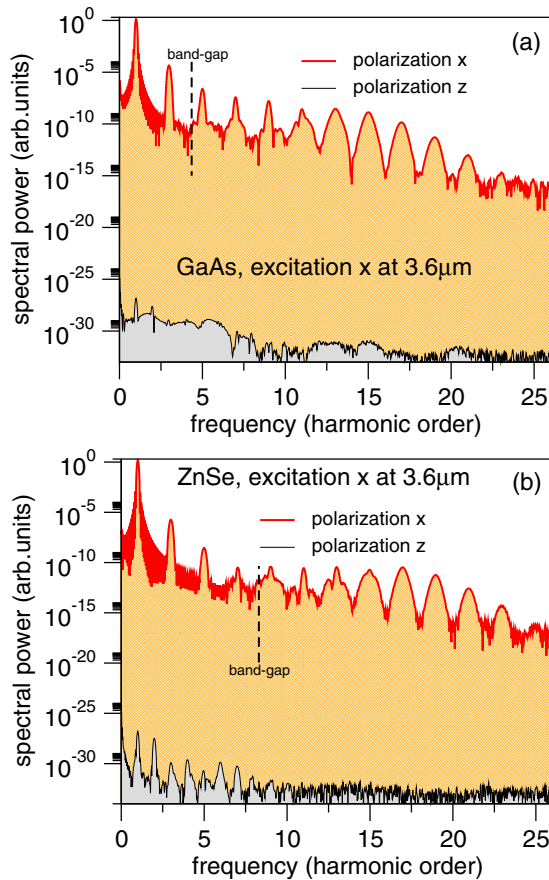

FIG. 3. High-order harmonic generation in 110-oriented GaAs crystal. Linearly polarized excitation pulse oscillates at 45 degrees with respect to the crystal axis. In this geometry, both even and odd harmonics should appear in the p as well as in the s polarization.

FIG. 6. Lineouts through the first Brillouin zone are shown in dashed red lines. The XΓX path is often used to simulate HHG from materials such as GaAs. We wish to visualize the contribution of different points along the lineout and see how they change when moving away from the center of the zone to, say, the WW lineout. The arrows indicate the direction of the excitation (E) and induced current components (J_x, J_z) corresponding to the components shown in Fig. 5.

FIG. 5. High-order harmonic generation in crystals excited by a linearly polarized pulse oscillating along the (crystal) x direction. In this geometry, the current density in the perpendicular direction (y, z) must vanish due to the material symmetry.

(b) different portions of the zone give rise to radiation with various phase shift and significant cancellation occur between them.

These illustrations also elucidate how it happens that the second-harmonic signals are absent in Fig. 5.

Let us consider a lineout of the Brillouin zone, for example a line of **k** vectors connecting two W points at the opposite sides of the Brillouin zone, or the X-Γ-X path going through the center of the zone, as depicted in Fig. 6. Black arrows indicate the polarization direction of the electric field, and of the parallel (J_x) and perpendicular (J_z) components of the induced current.

We calculate $\rho(\mathbf{k}; t)$ for each point of such a lineout and evaluate the corresponding current density as the trace with $\partial_\mathbf{k} h(\mathbf{k})$ as required by (5). The result is a contribution to the current which originates in the electronic states starting their evolution at a point of the lineout. We aim to compare the "strength of the response" between different regions of the reciprocal space.

Instead of the HHG spectrum, we visualize the induced current density because in this way one can appreciate different phase shifts and see how various contributions can interfere. To make figures easier to read we assume a shorter pulse, 50 fs duration, and we filter out the second-harmonic
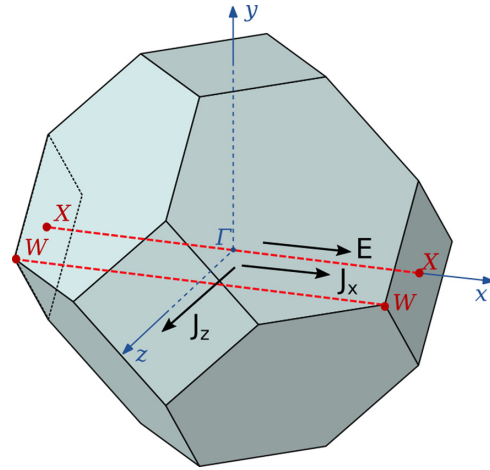
contribution from the current density. Then we plot a two-dimensional map of the current versus time and the initial **k** location along the selected lineout.

To elucidate the mechanism behind the vanishing second harmonics in Fig. 5. we first consider the z polarization output shown in Fig. 7 for the lineouts XΓX (top) and WW (bottom). What the top plot shows is merely numerical noise, so we can see that the points along XΓX do not generate the s-polarized second-harmonic contributions at all. However, moving away from the axis of the Brillouin zone to the line WW (bottom panel), one can see that every point gives a strong individual contribution. It is because the middle and outer portions of the lineout are out of phase that the total second harmonic vanishes in the end.

The mechanism that extinguishes the second harmonic for the polarization along the electric-field direction [cf. absent second-harmonic peak in the red (top) lines in Fig. 5] is similar and is illustrated in Fig. 8. This time we see strong contributions along both lineouts, but different regions in the reciprocal space exhibit out-of-phase contributions that interfere destructively.

These results are merely examples which of course cannot provide a complete "map" of how different parts of the Brillouin zone contribute to the observed HHG. Nevertheless, they make it quite evident that all parts of the Brillouin zone contribute to the HHG output on a qualitatively equal footing, and only when they are added together does the correct picture emerge. It is obvious that for a sample rotated with respect to that in the above example, the resulting strength of the harmonics of different polarization will sensitively reflect the interference between different parts of the Brillouin zone.

Our results also suggest that it is not given that the observed response is dominated by the initial **k** states with the strongest transition dipoles. Indeed, the **k** dependence of the signal
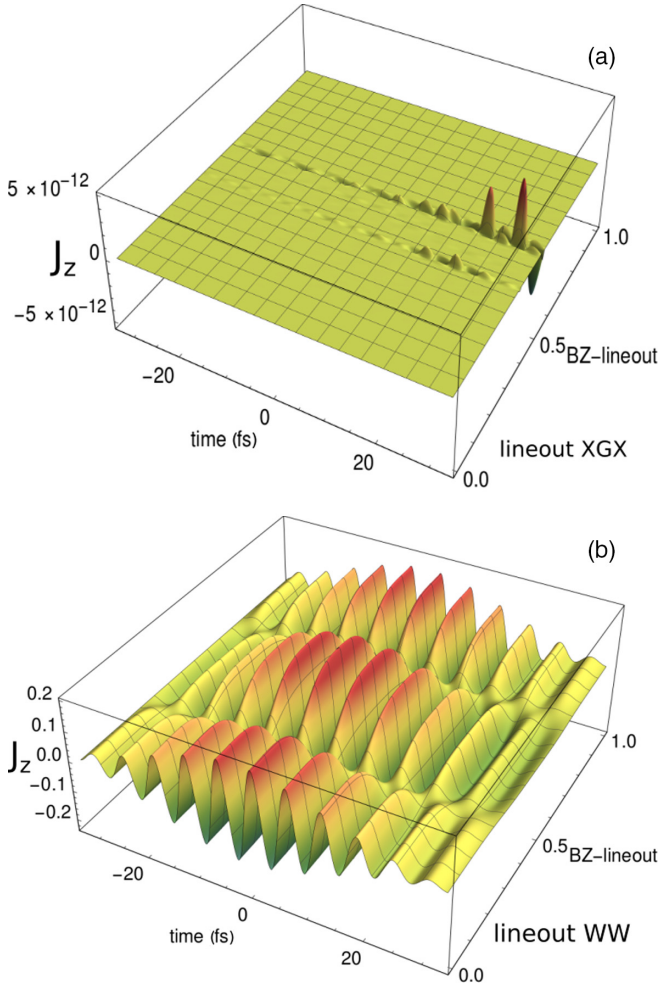
FIG. 7. The vector component of the time-dependent current density perpendicular to the driving electric field. Shown here is the filtered second harmonics in arbitrary units as a function of the initial **k** vector localized along the indicated lineout (dashed red line in Fig. 6) of the Brillouin zone. The lineout axis is in relative units.

FIG. 8. Time-dependent current density as in Fig. 7, but for the current-density vector component parallel to the electric field.

amplitudes in Figs. 7 and 8 does not follow the magnitude of the dipole moments which tend to be strongest in the vicinity of the Γ point. To emphasize this even more, Fig. 9 shows an example for a crystal sample with 110 orientation rotated about the beam by 90 (top panel) and 45 (bottom panel) degrees. While in this case the response from different **k** location appears to be in phase, the bottom panel shows that the strongest response depends on the polarization; when in the upper panel it is correlated with the strongest dipoles in the center, and the lower panel exhibits an asymmetry which is "out of sync" with the magnitude of the local transition dipoles. Moreover, it becomes evident that this particular Brillouin zone lineout should not be considered in isolation from its counterparts related by the crystal symmetry.

We therefore contend that the integration over the entirety of the Brillouin zone should be the default approach preferred over the numerically less intensive investigations restricted to low-dimensional subsets in the reciprocal space.
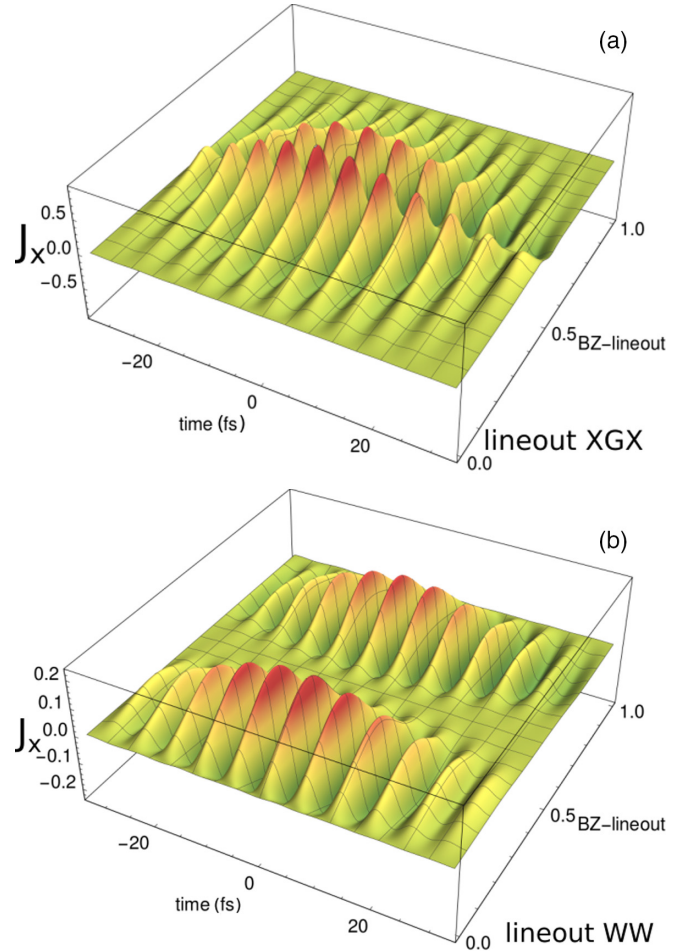
VI. CONCLUSIONS

We have presented an approach to the high-order harmonic generation from crystalline solid-state media which is completely free of any considerations related to the complex phases of the elements of the transition-dipole moment. In fact, the method does not require calculations of the transition dipole matrices which is a distinct advantage by itself. The simulation algorithm is informed by the fact that the absolute phases of these quantities are not physical observables, and the method is "phase blind" by design in the sense that it can work with arbitrary phases assigned to the Hamiltonian eigenstates. In particular, there is no requirement of differentiability or even continuity between the Hamiltonian bases used at "mutually close" points of the Brillouin zone. As such, our approach offers the best possible solution to the so-called transition-dipole phase problem by eliminating the issue entirely.

The method is computationally efficient and admits a perfectly-load-balanced parallelization. The speed is sufficient for future integration with the pulse-propagation simulators such as our gUPPE [48], making the spatially resolved studies of propagation effects in solid-state HHG feasible with the account of the whole Brillouin zone.
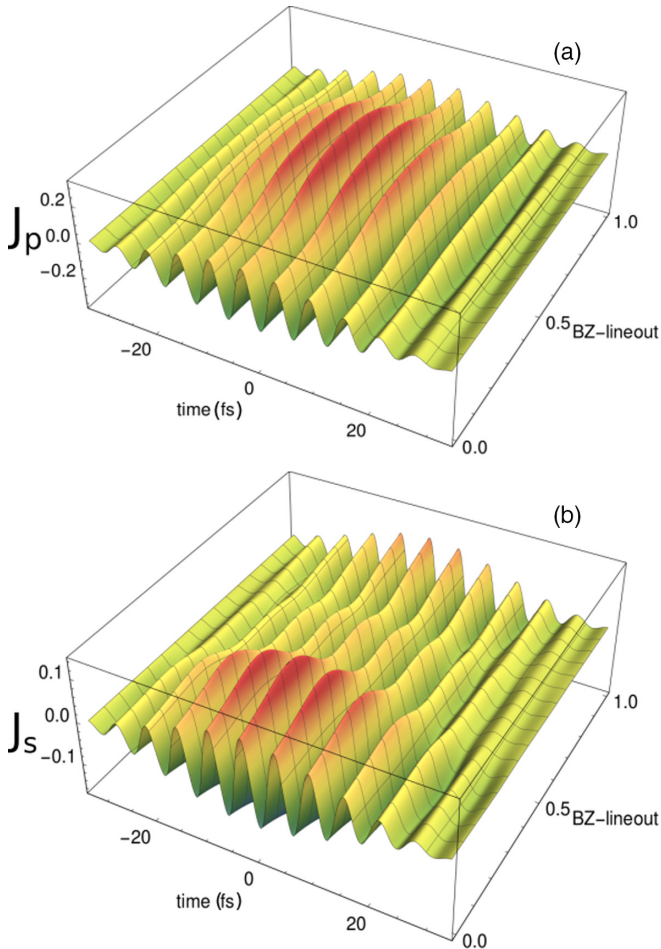
FIG. 9. Time-dependent current density (in arbitrary units) for the WW lineout (red dashed line in Fig. 6) and 110-oriented crystal sample. The top panel shows the p-polarized response for the sample rotated by 90 degrees, while the lower panel is for the s-polarized response and sample rotated by 45 degrees. It is obvious that the induced current amplitude is not always correlated with the local magnitude of the transition dipoles, which are strongest in the middle of the lineout.

It is actually relatively easy to integrate all induced current-density contributions over the whole three-dimensional Brillouin zone. This is shown crucial for the preservation of the material symmetry. Once the initial model utilized to calculate the band structure of the crystalline medium properly reflects the space-group of the material, the simulated HHG signals and in particular their sample-orientation and pulse-polarization dependencies are guaranteed to be correct.

We have shown that, in general, the entire Brillouin zone contributes to the high-order harmonic signal. This is perhaps not so surprising, but our simulation examples also demonstrate that there are considerable cancellations, or destructive interference between the contributions originating from the quantum states in different sectors of the Brillouin zone. It is therefore unrealistic to expect that, for a general sample orientation and excitation-pulse polarization, one could use a low-dimensional subset of the Brillouin zone to capture the high-order harmonic generation very accurately. We have also

seen that the strength of the transition-dipoles is not a reliable predictor of which part of the Brillouin zone may dominate the HHG signal.

These observation may have an important impact on some applications of solid-state HHG, such as Berry curvature measurement [9]. For example, all-optical band-reconstruction [4,5] and dipole-reconstruction [7] methods tend to utilize a one-dimensional picture of the reciprocal space by selecting a presumably dominant contribution to the process [6]. In contrast, here we have seen how the HHG-source can "light up" the Brillouin zone in rather nonintuitive patterns. We therefore believe that the full-Brillouin-zone simulations similar to those presented in our work can be a useful tool to identify the dominant channels in the high-order harmonic generation from crystalline materials.

Sampling the entire Brillouin zone with high resolution and being able to do it many times for various parameter scans, opens a door for a number of exciting investigations. Of particular interest is looking at the role of distinct features in the material band-structure, for example band-gaps between adjacent conduction bands [28], or spectral caustics associated with critical points in the energy bands [29]. These and other features can be studied in detail by mapping the HHG source around them (together with their symmetry-related partners) and comparing the signal to that from the complement in the Brillouin zone. This way one can determine the relative strength of the feature and probe for possible interference effects.

It is now feasible to simulate complex driving waveforms and study the polarization properties [34,49] of the harmonic signal [35]. Driving HHG with complex-polarization and multicolor pulses has been very fruitful in gases, and it will surely be even richer in the solid state. We believe that simulations and specifically those that can guarantee correct symmetry properties will be vital.

The high numerical fidelity of the proposed method invites a detailed investigation into the still-unresolved issue of dephasing. It is a well-known fact among practitioners that numerically simulated HHG spectra require unphysically short dephasing times, otherwise they would not compare well with experiments. While propagation effects [13,18] and spatial filtering [50] were proposed as a partial explanation, alternative dephasing mechanisms [51] were also considered, and one could argue that many-body effects should be included in the models. We suspect that the quality of the numerical data can also play a role, and it will be important to rule out possible artifacts.

Last but not least, we are approaching the stage when it will be possible to determine the absolute scale of the simulated HHG, and thus push the experiment-theory comparison much more in the quantitative direction [32]. The beauty of a HHG simulation with the full Brillouin zone is that it encompasses the response in the low-harmonic region where it can be quantitatively compared with measurements. For example, nonlinear coefficients and multiphoton absorption cross sections can be extracted from the HHG models and serve as benchmarks for accuracy. In turn, such quantitatively "anchored" simulations will motivate better, calibrated experiments.

APPENDIX: PRE-CALCULATING MATERIAL-MODEL DATA

This Appendix is intended for readers who may want to use DFT-generated material data, but for whatever reason do not wish to postprocess the *ab initio* calculations into an effective tight-binding model (e.g., via the maximally localized Wannier functions approach [31,46]). Is it possible to precalculate all that is necessary to avoid repeated, on-the-fly exact diagonalization? The purpose of this Appendix is to sketch in broad strokes how this could be done.

Let us assume that the material band-structure was solved for each point on a suitably chosen grid which samples the Brillouin zone. This means that eigenenergies and the eigenvectors are available at the grid points, but not for locations in between. For simplicity of the following discussion, we consider a linearly polarized electric field and a k grid in which one dimension aligns with the field direction.

For the initial density matrix $\rho(k, t = 0)$ for a fixed k, at time t_1 the algorithm has just calculated the state of the system for the **k** vector $k_1 = k - A(t_1)$, so the Hamiltonian basis is now known at this point even if it does not belong to the presampled grid. Let k_g be the nearest grid point in the direction of the driving field. The basis at k_g was precalculated and stored before the simulation so it can be retrieved, and we can readily construct the unitary transformation matrix $U^{1 \to g}$ as in Eq. (7).

Now let us say that, during the next integration step, the vector potential takes us from k_1 to $k_2 = k - A(t_2)$, and this is where we need to calculate the Hamiltonian eigenbasis. More precisely, what we require is the unitary transformation matrix $U^{1 \to 2}$ which takes the basis at k_1 and produces the basis at k_2. However, we wish to avoid running an exact-diagonalization routine anew, because it is expensive. Instead

we interpolate between the two unitary matrices, $U^{1 \to 1}$ (which is an identity) and $U^{1 \to g}$ to obtain $U^{1 \to 2}$. For this purpose, let us consider the "fractional distance" $f = (k_2 - k_1)/(k_g - k_1)$ representing how far k_2 is from k_1 when moving toward k_g. The interpolated transformation matrix corresponding to this fractional distance can be constructed as

$$U^{1 \to 2} = \text{MatExp}[f \, \text{MatLog}[U^{1 \to g}]], \quad (A1)$$

where MatExp and MatLog are matrix exponential and matrix logarithm functions, respectively. MatLog is the natural logarithm so it is the inverse function to MatExp. Both functions can be defined through their series expansions which only require matrix multiplication. Formula (A1) is called geodesic interpolation of unitary matrices [52]. Viewed as an f-parametrized family of matrices, this formula constructs the shortest path (in the sense of the Frobenius norm) between an identity matrix $U^{1 \to 1}$ and the unitary matrix $U^{1 \to g}$. We just need to select the value of f which brings us to the "location" k_2. Important for our application is that the interpolation matrix is guaranteed to be unitary.

Formula (A1) may not look friendly, but it is in fact easy to use. There is a number of good algorithms to obtain logarithms of unitary matrices in general [53], and in this particular case even the series-expansion method with only a few terms will suffice. Moreover, because the norm of MatLog$[U^{1 \to g}]$ will be small (here we assume a fine-resolution grid, of course), the evaluation of the matrix exponential is also easy, for example with the scaling-and-squaring method [54].

We have tested the unitary-matrix interpolation (A1) with the tight-binding models for the zinc-blende structure, both with and without spin-orbit coupling included. We have found that the procedure can be implemented so that it is fast and accurate even on coarsely sampled grids (e.g., with mere 16 points in each dimension). This approach is therefore a good candidate for using precalculated material data, such as from DFT, with the algorithm put forward in this work. Precalculation with subsequent interpolation on the fly may be suitable also for tight-binding models with larger dimensions; say, beyond twenty.

[1] S. Ghimire, A. D. DiChiara, E. Sistrunk, P. Agostini, L. F. DiMauro, and D. A. Reis, Nat. Phys. **7**, 138 (2011).

[2] E. Goulielmakis and T. Brabec, Nat. Photonics **16**, 411 (2022).

[3] J. Park, A. Subramani, S. Kim, and M. F. Ciappina, Adv. Phys.: X **7**, 2003244 (2021).

[4] G. Vampa, T. J. Hammond, N. Thiré, B. E. Schmidt, F. Légaré, C. R. McDonald, T. Brabec, D. D. Klug, and P. B. Corkum, Phys. Rev. Lett. **115**, 193603 (2015).

[5] J. Chen, Q. Xia, and L. Fu, Phys. Rev. A **104**, 063109 (2021).

[6] A. A. Lanin, E. A. Stepanov, A. B. Fedotov, and A. M. Zheltikov, Optica **4**, 516 (2017).

[7] Y. Qiao, Y.-Q. Huo, S.-C. Jiang, Y.-J. Yang, and J.-G. Chen, Opt. Express **30**, 9971 (2022).

[8] S. Han, L. Ortmann, H. Kim, Y. W. Kim, T. Oka, A. Chacon, B. Doran, M. Ciappina, M. Lewenstein, S.-W. Kim, S. Kim, and A. S. Landsman, Nat. Commun. **10**, 3272 (2019).

[9] T. T. Luu and H. J. Wörner, Nat. Commun. **9**, 916 (2018).

[10] C. Yu, S. Jiang, and R. Lu, Adv. Phys.: X **4**, 1562982 (2019).

[11] L. Yue and M. B. Gaarde, J. Opt. Soc. Am. B **39**, 535 (2022).

[12] L. Plaja and L. Roso-Franco, Phys. Rev. B **45**, 8334 (1992).

[13] I. Floss, C. Lemell, G. Wachter, V. Smejkal, S. A. Sato, X.-M. Tong, K. Yabana, and J. Burgdörfer, Phys. Rev. A **97**, 011401(R) (2018).

[14] M. Lindberg and S. W. Koch, Phys. Rev. B **38**, 3342 (1988).

[15] H. Haug and S. W. Koch, *Quantum Theory of the Optical and Electronic Properties of Semiconductors* (World Scientific Publishing, Singapore, 2009).

[16] M. Kira and S. W. Koch, *Semiconductor Quantum Optics* (Cambridge University Press, Cambridge, 2011).

[17] P. Xia, C. Kim, F. Lu, T. Kanai, H. Akiyama, J. Itatani, and N. Ishii, Opt. Express **26**, 29393 (2018).

[18] I. Kilen, M. Kolesik, J. Hader, J. V. Moloney, U. Huttner, M. K. Hagen, and S. W. Koch, Phys. Rev. Lett. **125**, 083901 (2020).

[19] X.-Y. Wu, H. Liang, X.-S. Kong, Q. Gong, and L.-Y. Peng, Phys. Rev. E **105**, 055306 (2022).

[20] M. Hussain, S. Kaassamani, T. Auguste, W. Boutu, D. Gauthier, M. Kholodtsova, J.-T. Gomes, L. Lavoute, D. Gaponov, N. Ducros, S. Fevrier, R. Nicolas, T. Imran, P. Zeitoun, G. O. Williams, M. Fajardo, and H. Merdji, Appl. Phys. Lett. **119**, 071101 (2021).

[21] U. Lindefelt, H.-E. Nilsson, and M. Hjelm, Semicond. Sci. Technol. **19**, 1061 (2004).

[22] J. Li, X. Zhang, S. Fu, Y. Feng, B. Hu, and H. Du, Phys. Rev. A **100**, 043404 (2019).

[23] D. Wu, L. Li, Y. Zhan, T. Huang, H. Cui, J. Li, P. Lan, and P. Lu, Phys. Rev. A **105**, 063101 (2022).

[24] S. Jiang, H. Wei, J. Chen, C. Yu, R. Lu, and C. D. Lin, Phys. Rev. A **96**, 053850 (2017).

[25] S. Jiang, J. Chen, H. Wei, C. Yu, R. Lu, and C. D. Lin, Phys. Rev. Lett. **120**, 253201 (2018).

[26] S. Jiang, C. Yu, J. Chen, Y. Huang, R. Lu, and C. D. Lin, Phys. Rev. B **102**, 155201 (2020).

[27] K. Kaneshima, Y. Shinohara, K. Takeuchi, N. Ishii, K. Imasaka, T. Kaji, S. Ashihara, K. L. Ishikawa, and J. Itatani, Phys. Rev. Lett. **120**, 243903 (2018).

[28] A. J. Uzan-Narovlansky, A. Jiménez-Galán, G. Orenstein, R. E. F. Silva, T. Arusi-Parpar, S. Shames, B. D. Bruner, B. Yan, O. Smirnova, M. Ivanov, and N. Dudovich, Nat. Photon. **16**, 428 (2022).

[29] A. J. Uzan, G. Orenstein, A. Jiménez-Galán, C. McDonald, R. E. F. Silva, B. D. Bruner, N. D. Klimkin, V. Blanchet, T. Arusi-Parpar, M. Krüger, A. N. Rubtsov, O. Smirnova, M. Ivanov, B. Yan, T. Brabec, and N. Dudovich, Nat. Photon. **14**, 183 (2020).

[30] K. Imasaka, Y. Shinohara, T. Kaji, K. Kaneshima, N. Ishii, J. Itatani, K. L. Ishikawa, and S. Ashihara, Opt. Continuum **1**, 1232 (2022).

[31] R. E. F. Silva, F. Martín, and M. Ivanov, Phys. Rev. B **100**, 195201 (2019).

[32] S. Ghimire and D. A. Reis, Nat. Phys. **15**, 10 (2019).

[33] P. Xia, T. Tamaya, C. Kim, F. Lu, T. Kanai, N. Ishii, J. Itatani, H. Akiyama, and T. Kato, Phys. Rev. B **104**, L121202 (2021).

[34] S. Kaassamani, T. Auguste, N. Tancogne-Dejean, X. Liu, W. Boutu, H. Merdji, and D. Gauthier, Opt. Express **30**, 40531 (2022).

[35] N. Klemke, N. Tancogne-Dejean, G. M. Rossi, Y. Yang, G. DiSciacca, A. Rubio, F. Kärtner, O. Mücke, F. Scheiba, and R. Mainz, Nat. Commun. **10**, 1319 (2019).

[36] J. Wilhelm, P. Grössing, A. Seith, J. Crewse, M. Nitsch, L. Weigl, C. Schmid, and F. Evers, Phys. Rev. B **103**, 125419 (2021).

[37] S. C. Liebscher, M. K. Hagen, J. Hader, J. V. Moloney, and S. W. Koch, Phys. Rev. B **104**, 165201 (2021).

[38] H. Liu, Y. Li, Y. S. You, S. Ghimire, T. F. Heinz, and D. A. Reis, Nat. Phys. **13**, 262 (2017).

[39] G. Vampa, C. R. McDonald, G. Orlando, D. D. Klug, P. B. Corkum, and T. Brabec, Phys. Rev. Lett. **113**, 073901 (2014).

[40] G. Carcassi, L. Maccone, and C. A. Aidala, Phys. Rev. Lett. **126**, 110402 (2021).

[41] L. Masanes, T. D. Galley, and M. P. Müller, Nat. Commun. **10**, 1361 (2019).

[42] M. Suzuki, Phys. Lett. A **146**, 319 (1990).

[43] P. Vogl, H. P. Hjalmarson, and J. D. Dow, J. Phys. Chem. Solids **44**, 365 (1983).

[44] Ö. Akinci, H. H. Gürel, and H. Ünlü, Thin Solid Films **517**, 2431 (2009).

[45] A. D. Carlo, Semicond. Sci. Technol. **18**, R1 (2003).

[46] I. Souza, N. Marzari, and D. Vanderbilt, Phys. Rev. B **65**, 035109 (2001).

[47] J. Ibañez-Azpiroz, F. de Juan, and I. Souza, SciPost Phys. **12**, 070 (2022).

[48] M. Kolesik and J. V. Moloney, Phys. Rev. E **70**, 036604 (2004).

[49] D. Baykusheva, A. Chacón, J. Lu, T. P. Bailey, J. A. Sobota, H. Soifer, P. S. Kirchmann, C. Rotundu, C. Uher, T. F. Heinz, D. A. Reis, and S. Ghimire, Nano Lett. **21**, 8970 (2021).

[50] C. Q. Abadie, M. Wu, and M. B. Gaarde, Opt. Lett. **43**, 5339 (2018).

[51] G. G. Brown, A. Jiménez-Galán, R. E. F. Silva, and M. Ivanov, arXiv:2210.16889.

[52] R. Movassagh, arXiv:1810.04681.

[53] T. A. Loring, Numer. Linear Algebra Appl. **21**, 744 (2014).

[54] C. Moler and C. V. Loan, SIAM Rev. **45**, 3 (2003).